Structure of Merger Remnants: IV. Isophotal Shapes

Jeremy S. Heyl* Lars Hernquist† David N. Spergel‡

19 October 1993

Abstract

This paper examines the shapes of isophotes of galaxy–merger remnants. More specifically, we perform a series of numerical experiments to study galaxy mergers. The simulations explore a variety of encounter geometries, types of progenitor galaxies, and particle number. We "observe" each of the remnants from sixty–four viewpoints to estimate how the isophotal shapes vary with the orientation of the remnant. Also, by comparing the results from the various simulations, we learn how encounter geometry and the structure of the progenitors can affect the shape of the remnants. The encounter geometry, the structure of the progenitors, and the orientation of the remnant play deciding roles in the shape of the "observed" isophotes, so much so that these simulated merger remnants have both "boxy" and "disky" isophotes and ellipticities ranging from E0 to E7. Thus, the shapes seen in our merger simulation remnants span a similar range to observed isophotal shapes of real galaxies.

Furthermore, to estimate the errors in this analysis, we introduce the statistical bootstrap. Bootstrapping is used rather widely in observational astronomy when dealing with small samples; however, its use is practically unheard of for tackling theoretical problems. We believe that bootstrapping can be extremely useful for dealing with the small samples found in numerical simulations; therefore, we present the rudiments and basis of the technique with emphasis on its use in N–body calculations. Also, by comparing the errors for the smaller simulations with those of the larger ones, we speculate on the number of particles required to accurately explore isophotal shapes in simulations.

Subject headings: galaxies: interactions, galaxies: structure, methods: numerical

*Department of Physics, South Road, University of Durham, Durham DH1 3LE, United Kingdom and Princeton University Observatory, Princeton, New Jersey 08540 USA

†Sloan Foundation Fellow, Presidential Faculty Fellow; Lick Observatory, U.C. Santa Cruz, Santa Cruz, California 95064 USA

‡Sloan Foundation Fellow, Presidential Young Investigator, Princeton University Observatory, Princeton, New Jersey 08540 USA

1 Introduction

Numerical simulations suggest that a wide range of initial conditions can lead to the formation of stellar systems that look roughly like early type galaxies (see, de Zeeuw and Franx 1991 for a review). This weak connection between formation mechanism and final state is a reflection of the effectiveness of violent relaxation in erasing the galaxy's memory of its initial conditions. Fortunately, violent relaxation is not completely effective, thus, detailed observations of the kinematics and photometry of elliptical galaxies can potentially yield information about their origin.

The merger hypothesis for the origin of elliptical galaxies (Toomre & Toomre 1972, Toomre 1977) proposes that the early-type stellar systems form through the merger of spirals and other "late-type" systems. In this paper, we explore this "merger" hypothesis by comparing the the remnants of numerical simulations of galaxy mergers to the observed characteristics of elliptical galaxies and the details of their light distribution, in particular, the ellipticity of their isophotes and their deviations from ellipticity. To this end, we have performed a series of twelve simulations exploring a variety of initial orbital characteristics (prograde, retrograde and skew encounters), models for the progenitors (bulgeless disks and others with non-rotating or rotating bulges) and particle number (between 65,000 and 300,000).

Elliptical galaxies are among the most widely studied objects in astronomy and have been found to possess a well–defined set of properties. Twenty years ago ellipticals were thought to be nearly featureless distributions of stars with almost perfect elliptical symmetry; the only descriptive parameter of their shape was ellipticity. Their scale was thought to be determined simply by their velocity dispersion, and their flattening was thought to be caused by simple rotation. Furthermore, ellipticals were believed to have a universal distribution of surface brightness – the de Vaucouleurs or $r^{1/4}$ law (de Vaucouleurs 1948). This was the state of affairs when Toomre & Toomre (1972) argued that mergers result in featureless piles of stars.

However, things did not remain this simple for long. Soon observing techniques advanced to the point that astronomers could actually measure the rotation of elliptical galaxies. They found that ellipticals rotate at one–third of the rate necessary to explain their flattening (Bertola & Capaccioli 1975; Illingworth 1977). Our general understanding has become more detailed since then. In 1987 the scatter in the original Faber–Jackson scaling relation was explained in terms of the Fundamental Plane and the $D_n - \sigma$ relation (Djorgovski & Davis 1987; Dressler *et al.* 1987) – a linear family (with some scatter) was replaced by a planar one.

Almost simultaneously, the fine structure of elliptical galaxies was being uncovered. Franx & Illingworth (1990) and Peletier *et al.* (1990) measured color gradients from the center to the outskirts of elliptical galaxies; Rix & White (1992), Bender (1990), and Franx, Illingworth & Heckman (1989) explored the velocity distributions of these previously "uninteresting" objects; some normal–looking ellipticals were found to possess kinematic anomalies (*e.g.* Franx & Illingworth 1988; Bender 1998; Jedrzejewski & Schechter 1988), "shells," and/or X–structures (*e.g.* Malin & Carter 1980, 1983; Schweizer 1980; for a recent review, see *e.g.* Barnes & Hernquist 1992); Bender, Döbereiner, & Möllenhoff (1987) and Simien & Michard (1990) found that the isophotes of elliptical galaxies deviate from being perfect ellipses.

The "merger" hypothesis appeared during a simpler time in our understanding of elliptical galaxies, but it too has become more complicated and more subtle over the years. Not only have the simulations become more sophisticated, but so have our methods of analysis. The hypothesis must now attempt to explain not only the gross characteristics of elliptical galaxies but also some of their fine structure. Barnes (1992) and Hernquist (1992) found that remnants of simulated mergers possess $r^{1/4}$–laws and other global properties similar to those of elliptical galaxies. Furthermore, Hernquist, Spergel & Heyl (1993) argued that mergers may also explain various observed scalings between elliptical galaxies.

This paper shifts the focus from that of previous works. We examine the fine structure of merger remnants, rather than their global properties. This focus on fine structure requires larger simulations than earlier studies (*e.g.* Barnes 1988, 1992; Hernquist 1992). Here we consider the photometry of merger remnants and, by association, of elliptical galaxies: the isophotes and their deviations from ellipticity. A common speculation about the origin of these deviations is that galaxies after suffering an interaction are likely to exhibit "boxy" isophotes, while on the other hand elliptical galaxies with "disky" isophotes represent a bridge population between ellipticals and S0s (Bender *et al.* 1989, Nieto *et al.* 1991). More specifically, they argue that the sequence from S0s through disky ellipticals to boxy ellipticals traces a trend of mergers with decreasing dissipation.

Essentially, it has been proposed that these deviations may represent the key to understanding the origin of "early–type" galaxies. Recent simulations suggest that both galaxy mergers (Governato *et al.* 1993) and dissipationless collapse (Stiavelli *et al.* 1991) can produce both boxy and disky elliptical isophotes. This paper confirms their conclusion that the same merger remnant, when viewed from different orientations, can appear to have either boxy or disky isophotes. Some of the encounter geometries even result in remnants with essentially perfect elliptical isophotes (within the errors of our analysis). Thus, the experiments imply that mergers may not leave easily discovered tracers in the isophotes. As our simulations do not include dissipation, we cannot explore Bender *et al.*'s (1992, 1993) plausible hypothesis that dissipation plays an important role in the formation of disky isophotes. Furthermore, we cannot explain the observed contrasts between boxy and disky ellipticals such as x-ray activity, kinematics, and luminousity functions.

In the following sections, we describe the simulations (§ 2), the determination of the isophotes (§ 3.1) and their errors (§ 3.2). Later, we describe our results (§ 4) and discuss their implications (§ 5); finally, we make some concluding remarks (§ 6).

2 The Simulations

The simulations examined here are part of an ongoing series studying the nature of remnants produced by the mergers of galaxies resembling the Milky Way (Hernquist 1992; Hernquist & Spergel 1992; Spergel & Hernquist 1992; Hernquist 1993a; Hernquist, Spergel & Heyl 1993; Hernquist, Heyl & Spergel 1993). The gravitational self–interaction of the system is calculated with a hierarchical tree algorithm (Barnes and Hut 1986) which has been further optimized for use with vectorizing supercomputers (Hernquist 1987; Hernquist 1990a; Hernquist & Katz 1989). Rather than scaling as $\sim O(N^2)$ as with direct summation, the "tree" method scales as $\sim N\log(N)$, making possible simulations with upwards of a quarter of a million particles.

Before delving into a discussion of the initial conditions, a description of the units used throughout this paper is appropriate. In our system of units, G is set equal to 1 and after scaling to the Galaxy, the units of length, time and mass become respectively 3.5 kpc, 1.31×10^7 yr, $5.6\times 10^{10}\mathrm{M}_\odot$. A unit velocity then corresponds to 263.3 km/s. Each simulation evolves through 144 time units or 1.9×10^9 yr, and the first pericenters are reached approximately 24 time units after the beginning of the simulations.

The progenitor galaxies are modeled after the Milky Way with a thin disk of stars following the Bahcall–Soneira model (1980), *i.e.*

$$\rho_{disk}(R,z) \propto \exp(-R/h)\mathrm{sech}^2(z/z_0) \tag{1}$$

where R is the distance from the axis of rotation of the disk and z is the altitude above the disk's plane. We set the exponential scale length to 1 length unit (3.5 kpc) and choose 0.2 length units for the scale height. The stars travel on nearly circular orbits but have sufficient velocity dispersion to guarantee stability against the formation of bars, with the Toomre Q–parameter equal to 1.5 at 8 kpc, the solar radius. Each disk is embedded in a spherical dark–matter halo ($M_{\mathrm{halo}}=5.8$) so that the stars follow rotation curve similar to that of our Galaxy. The halos follow the profile: $\rho_{\mathrm{halo}} \propto \exp(-r^2/r_t^2)/(1+r/\gamma^2)$ with $r_t=10$ and $\gamma=1$. Some of the models also have bulges of mass one-third. The bulges follow flattened Hernquist (1990b) profiles:

$$\rho = \frac{M}{2\pi abcm(1+m)^3} \tag{2}$$

where

$$m^2 = \frac{x^2}{0.2^2}+\frac{y^2}{0.2^2}+\frac{z^2}{0.1^2}. \tag{3}$$

For the rotating bulges all the particles are forced to have the same sign of azimuthal velocity. Although this latter choice is far from ideal, it provides a convenient method for adding plausible amounts of net rotation to bulges. (See Hernquist 1993b for details.)

In each simulation the centers of mass of the galaxies are initially separated by 30 units on parabolic trajectories. The pericentric distance would have been 2.5, if they had followed Keplerian trajectories. The choice of parabolic encounters strikes a compromise (Barnes 1992) between the highly eccentric ($0 \ll e \leq 1$) or Toomre's (1977) loosely bound pairs and pairs that have been accelerated into hyperbolic orbits by a background distribution of dark matter. Although these choices of encounter geometries hardly sample the multi-dimensional space of possible interactions, they do represent a set of realistic and likely possibilities and probe its variety.

The simulations fall into two sets, one four times larger than the other. In the smaller simulations, 16,384 particles comprise each halo, 16,384 comprise each disk and 4,096 comprise each of the bulges if they are present, giving a total of 65,536 or 73,728 particles for the smaller simulations. The halos have a mass of 5.8. The disks and bulges have a mass ratio of three to one with the mass of each disk being unity. For the larger models, the particle number is simply increased by a factor of four in each component while holding the total masses and the ratios between components constant.

3 Analysis Techniques

The analysis may be divided into two steps. First, the simulations are converted into grey–scale "images" suitable for further analysis with customary image processing tools and the isophotes at various radii are extracted as described in § 3.1. The second step is to estimate the errors in the isophote analysis arising from the discreteness of the simulations. § 3.2 describes how the simulations are resampled and the errors estimated using a statistical bootstrap.

3.1 Isophote Derivation

The first step in deriving isophotes from a simulation is selecting the set of viewpoints from which to observe the remnant. In our case we choose sixty–four orientations which span one quadrant of a sphere, taking advantage of the approximate symmetries of the encounter. For each orientation, an image is created by counting all the particles in a square with 20 length units (70 kpc) on a side. For the smaller simulations a 200-by-200 pixel mesh is chosen to span the square while for the larger ones a 400-by-400 pixel mesh is used. The number of particles that fall within each pixel becomes the grey–scale value for that pixel. Thus, we create a false CCD image of the remnant, and the mean signal-to-noise ratio for each pixel is approximately constant between the simulations regardless of size (the simulations with bulges have a slightly higher signal-to-noise ratio).

Unfortunately, we are not dealing with real CCD images of galaxies, else we could simply use available software to derive isophotes; however, the signal-to-noise ratio per pixel of the simulated images has a peak of approximately ten in the brightest core of the image, compared to values ten and more times higher than this in CCD images of elliptical galaxies. We attempted to use the `ISOPHOTE` routines within the `STSDAS` package of IRAF, but the algorithm does not always converge, and furthermore its errors quickly increase with the level of noise.

Instead we sample a larger portion of the image than usual algorithms and employ a hybrid method to calculate the residuals. The center of all the isophotes in an image is assumed to coincide with the center of brightness of the entire image — this assumption reduces the number of parameters by two and consequently increases our chances for success. An isophote is found by progressively iterating an elliptical path (with an optional "boxy" or "disky" deviation) through the image to minimize the root-mean-squared variation along the path. This not only gives an estimate of the ellipticity but also of the boxiness or diskiness of the isophote. Once the isophote is derived we can reestimate the $\cos 4\theta$ deviations by fitting a linear combination of $\cos 4\theta$ and $\sin 4\theta$ to the residuals along the path (without a boxy/disky addition) as IRAF does (Jedrzejewski 1987). For a clean image, if we fit

$$I = I_0 + A_4 \cos(4\theta) + B_4 \sin(4\theta) \tag{4}$$

along the best-fit elliptical isophote, an estimate of the deviation in the path of the isophote is

$$\zeta_{\cos 4\theta} = -\frac{A_4}{RI'(R)}. \tag{5}$$

where $I'(R)$ is the radial intensity gradient at the isophote. The result for the sine term is analogous. When tested on noiseless, false images, both these techniques gave values for all the parameters of the elliptical isophotes and their deviations which agree with those of IRAF within IRAF's quoted errors. However for images with noise levels similar to those of the simulations, the errors were much smaller for the best–fit path method; therefore, we decide to use the cosine term found from finding the best–fit path and to discard information about the sine term (B_4 in Equation 4). We use the notation, $\zeta_{\cos 4\theta}$ (instead of the usual a_4) to designate the deviation of an isophote's path from ellipticity.

Each of the images is smoothed with a Gaussian filter of standard deviation one pixel, and then the isophotes are derived at $0.5r_e$, $1.0r_e$ and $1.5r_e$ where r_e is the radius of the circular aperture containing half the light of the remnant. For each isophote, the parameters of interest are $\epsilon = 1 - b/a$, the ellipticity, and $\zeta_{\cos 4\theta}$, the boxiness/diskiness parameter. An isophote with a negative value of $\zeta_{\cos 4\theta}$ appears boxy and conversely one with a positive value appears disky.

3.2 The Bootstrap

The statistical bootstrap, the cousin of the Quenouille-Tukey jackknife, was introduced by Efron in 1977 (Efron 1979). It most often makes its appearance in astronomy when estimating errors and biases in small samples especially those in the study of large-scale structure (Nobelis 1990; Bhavsar 1990), recently, bootstrap techniques have been applied to studies of Lyman alpha clouds (Press *et al.* 1993); what is less commonly known is that the bootstrap lies at the very basis of using N–body simulations to trace the evolution of the Boltzmann equation. In this section we introduce or rather reintroduce the bootstrap and outline how we use it to estimate the errors in our derived ellipticities and $\cos 4\theta$ residuals (Refer to Lupton 1993 for further details).

An N–body simulation traces the evolution of a dynamical system by drawing a sample of n independent points $\{(\vec{x}_i, \vec{v}_i)\}_0$ from the phase–space distribution function, $f(\vec{x}, \vec{v}, t_0)$. Then the simulation calculates the evolution using Newton's equations with an appropriate smoothing technique. The final product is another sample of n points $\{(\vec{x}_i, \vec{v}_i)\}$ from a phase–space distribution function which we assume to be approximately equal to $f(\vec{x}, \vec{v}, t_f)$, the true evolved distribution function. The next step is to calculate some statistic for the simulation: for example, the position along the z–axis of the center of mass:

$$z_{\mathrm{CM}} = \bar{z} = \frac{1}{n} \sum_i z_i \tag{6}$$

and its associated error

$$\sigma_z^2 = \frac{1}{n} \frac{1}{n-1} \sum_i (\bar{z} - z_i)^2. \tag{7}$$

By performing these summations, we assumed that the statistics of the set $\{(\vec{x}_i, \vec{v}_i)\}$ are a good approximation to those of the actual phase–space distribution function, $f(\vec{x}, \vec{v}, t_f)$. This is the assumption behind statistical bootstrapping.

However, we could have taken a more complicated route and created another distribution function,

$$f^* = \frac{1}{n} \sum_i \delta(\vec{x} - \vec{x}_i, \vec{v} - \vec{v}_i), \tag{8}$$

and then calculated center of mass by taking the integral,

$$z_{\mathrm{CM}} = \int z f^* d\vec{x} d\vec{v}. \tag{9}$$

Now we have two methods to calculate the error in our calculation for the center of mass: calculating an integral analogous to the second summation

(Equation 7), or drawing a variety of samples from our new distribution function f^* and investigating the distribution of $z^*_{\rm CM}$. Our original sample, $\{(\vec{x}_i, \vec{v}_i)\}$, is now only one of many possible realizations of f^*, and the distribution of $z^*_{\rm CM}$ over the various resamplings approximates the distribution of $z_{\rm CM}$ over f^* (Lupton 1993) which we in turn assume to approximate $f(\vec{x}, \vec{v}, t_f)$. Thus, through resampling we can estimate the error in our determination of $z_{\rm CM}$ given by Equation 7.

When we draw a sample from f^*, we must pick n values, specifying the number of copies n_i of each $\{(\vec{x}_i, \vec{v}_i)\}$ we have in the new sample. The n_i follow a multinomial distribution with $p_i = 1/n$, so

$$< n_i >^* = 1 \tag{10}$$

and

$$< n_i n_j >^* = 1 + \delta_{ij} - 1/n. \tag{11}$$

For each of the j samples the $z_{{\rm CM},j} = 1/n \sum n_{ij} z_i$, and therefore $< z_{\rm CM} >^* = 1/n \sum z_i$ as in Equation 6; in other words $z^*_{\rm CM}$ is unbiased. More interesting to us is the variance.

$$\begin{aligned} V^*(z_{\rm CM}) &= < z^2_{\rm CM} >^* - < z_{\rm CM} >^2 \\ &= \frac{1}{n^2} \sum_{ij} < n_i n_j >^* z_i z_j - \bar{z}^2 \\ &= \frac{1}{n^2} \sum_i z_i^2 + \left(1 - \frac{1}{n}\right) \sum_{ij} \left(\frac{1}{n} \sum_i z_i\right)^2 - z^2_{\rm CM} \\ &= \frac{1}{n} \left(\frac{1}{n} \sum_i z_i^2 - z^2_{\rm CM}\right) \\ &= \frac{1}{n} s^2 \end{aligned} \tag{12}$$

which is essentially the same as Equation 7.

This Monte–Carlo resampling is less expedient than using Equation 7, but often we do not have the luxury of a statistic defined as simply as $z_{\rm CM}$ is in Equation 6 and even more rarely do we have the luxury of a straightforward analytic error estimator like Equation 7. Rather, the interesting statistic may have to be calculated with an iterative algorithm with complicated errors such as the isophote derivation described in § 3.1.

So how is the bootstrap implemented with numerical simulations? Ordinarily when one calculates a physical value from a simulation, one uses all the particles, counting each once. To use the bootstrap, one simply needs to select from an n–particle simulation n particles *with replacement.* For example, in our 262,144–particle simulation, half the particles are considered luminous (the rest trace the dark matter). To create a bootstrapped image, we uniquely labeled each of the luminous particles with a number from 1 to 131,072. We then selected 131,072 numbers from 1 to 131,072 and used the particles with the appropriate labels to create a new ensemble. Some of the particles in the original simulation are included in the new ensemble several times and others not at all. Then the positions of the particles in this new group are projected as described in § 3.1 to create a bootstrapped image. By comparing the results of the fitting algorithm for a set of images bootstrapped from the same remnant from at the same viewpoint, we can easily estimate the error in all the isophote parameters by means of Equation 12.

When the bootstrap is applied to our isophote–deriving algorithm, we find some interesting results. First, as mentioned earlier, the current algorithm outperforms that of IRAF by a factor of 3 in the derivation of the fourth–order cosine term and by a factor of 2 in deriving the ellipticity of the isophotes. Combined with the fact that IRAF does not always successfully converge to a result, this is why we elected to develop this alternative algorithm. However, even after finding a method optimized for our noisy images, the errors are not a small as one would hope, but they do point to a method for later improvement.

For the 256–thousand–particle simulations, our error estimates fall in two groups. For the remnants that resulted from mergers of bulgeless galaxies, the error estimates are consistently higher than for those resulting from galaxies with bulges. We estimate the error in ellipticity for the first class to be about 0.1, thus an E4 resulting from a simulated merger of two bulgeless galaxies could be misclassified as an E5; the errors in the determination of $\zeta_{\cos 4\theta}$ are approximately 0.01. IRAF quotes errors of approximately 0.002 for "perfect" test images. For the second class, the results are better; the error in ellipticity is on average about 0.02 (E6.5 could actually be a E6.3) and in $\zeta_{\cos 4\theta}$ approximately 0.006, approaching IRAF's results on "perfect" test images. For the smaller simulations, the errors in ellipticity and boxiness were 2.0 and 1.7 times higher respectively. The errors decreased with decreasing ellipticity and boxiness/diskiness.

4 Results

The results from twelve simulations are presented here, exploring a variety of orientations and progenitor types; however, before examining the results, we must explain our shorthand for designating the various sets of initial conditions. The individual runs will be referred to with the following system of codes (two letters, followed by two numbers): `NB` and `RB` refer to "No Bulge" and "Rotating Bugle" respectively; each of the two numbers refers to one of the galaxies with `0`, `1`, `2` designating that its spin axis is aligned with the orbital angular momentum, is at approximately 71 degrees to the orbital axis and is anti–aligned with orbital angular momentum respectively. The run codes are summarized in Table 1

The isophotes for a given simulation may most concisely be represented by

Table 1: Run Codes

Run Code	Description
RB00	Both progenitors have rotating bulges and both disks rotate prograde with respect to the orbit.
NB02	Neither progenitor has a bulge, and one disk rotates retrograde.
NB01	Neither progenitor has a bulge, and one disk is tilted with respect to the orbit plane.
NB11	Neither progenitor has a bulge, and both disks are tilted with respect to the orbit plane.
RB11	Both progenitors have rotating bulges, and both disks are tilted with respect to the orbit plane.
NB22	Neither progenitor has a bulge, and both disks rotate retrograde.

the mean and standard deviation of the ellipticity and $\zeta_{\cos 4\theta}$ over the orientations as presented in Table 2 and Table 3. Several trends are evident with some examination of the tables. First, the remnants resulting from the smaller simulations are rounder and have isophotes that less closely follow ellipses. Second, in the mean, the isophotes at larger radii tend to be slightly less round than those at the half–light radii. Finally, few of the remnants are very boxy or disky in the mean, and by examining the distributions themselves or the deviations presented in Table 3, one can see that all the simulations resulted in both disky and boxy isophotes depending on the viewpoint. We also show more detailed results for the simulations `NB11` and `RB11`, which we believe have the most realistic initial conditions, in Figures 1 and 2. We examine the isophotes at one-half of an effective radius; it is here that isophotes are usually measured in elliptical galaxies. These simulations trace the evolution of a merger of two galaxies whose disk planes do not coincide with the plane of their mutual orbit. Furthermore, a comparison of the two figures reveals the effects of a bulge in the progenitor galaxies on the isophotes at one half of the half–light radius. Figure 3 depicts how $\zeta_{\cos 4\theta}$ changes with the inclination of the line of sight with respect to the initial orbital plane for `RB00` at 1 r_e. Whether a simulated merger remnant appears disky or boxy is a strong function of orientation.

By adding up the results from all of the simulations, we can estimate the residual "signal" that dissipationless merging leaves on the isophotes. As we have not determine which sets of the initial conditions are most likely, each simulation is weighted equally; consequently, the distributions in Figure 4 can only provide a thumbnail sketch of the properties of merger remnants in general (Figure 5 depicts similar data for a sample of observed ellipticals). In additional to the trends discussed in the previous paragraphs, a new feature appears in the distribution of $\zeta_{\cos 4\theta}$. Although most remnants are neither especially boxy nor

Table 2: Ellipticity Determinations – Means and Deviations

Run Code	0.5 r_e		1.0 r_e		1.5 r_e	
	Mean	σ	Mean	σ	Mean	σ
256–Thousand–Particle Simulations						
RB00	0.352	0.142	0.382	0.166	0.415	0.175
NB02	0.428	0.170	0.505	0.152	0.509	0.181
NB01	0.478	0.185	0.459	0.166	0.402	0.142
NB11	0.371	0.128	0.383	0.127	0.336	0.122
RB11	0.358	0.108	0.315	0.127	0.300	0.105
NB22	0.575	0.194	0.483	0.160	0.476	0.172
64–Thousand–Particle Simulations						
RB00	0.241	0.133	0.344	0.172	0.388	0.177
NB02	0.394	0.134	0.438	0.153	0.417	0.201
NB01	0.389	0.179	0.375	0.134	0.310	0.094
NB11	0.371	0.162	0.357	0.103	0.342	0.102
RB11	0.225	0.096	0.254	0.133	0.264	0.111
NB22	0.380	0.206	0.390	0.189	0.401	0.199

Table 3: Boxiness and Diskiness Determinations ($\zeta_{\cos 4\theta}$) – Means and Deviations

Run Code	0.5 r_e		1.0 r_e		1.5 r_e	
	Mean	σ	Mean	σ	Mean	σ
256–Thousand–Particle Simulations						
RB00	-0.002	0.006	-0.000	0.011	0.005	0.022
NB02	-0.004	0.017	-0.006	0.017	-0.002	0.012
NB01	-0.000	0.007	-0.014	0.012	-0.014	0.016
NB11	0.006	0.008	0.009	0.020	0.006	0.019
RB11	-0.003	0.007	-0.004	0.009	0.001	0.014
NB22	0.000	0.018	0.002	0.016	0.001	0.014
64–Thousand–Particle Simulations						
RB00	-0.003	0.017	0.002	0.012	-0.001	0.011
NB02	0.002	0.014	0.004	0.015	0.007	0.026
NB01	0.007	0.017	-0.003	0.009	0.002	0.014
NB11	0.006	0.014	0.022	0.033	0.017	0.028
RB11	0.003	0.011	0.003	0.008	0.010	0.011
NB22	-0.001	0.023	0.007	0.019	0.001	0.011

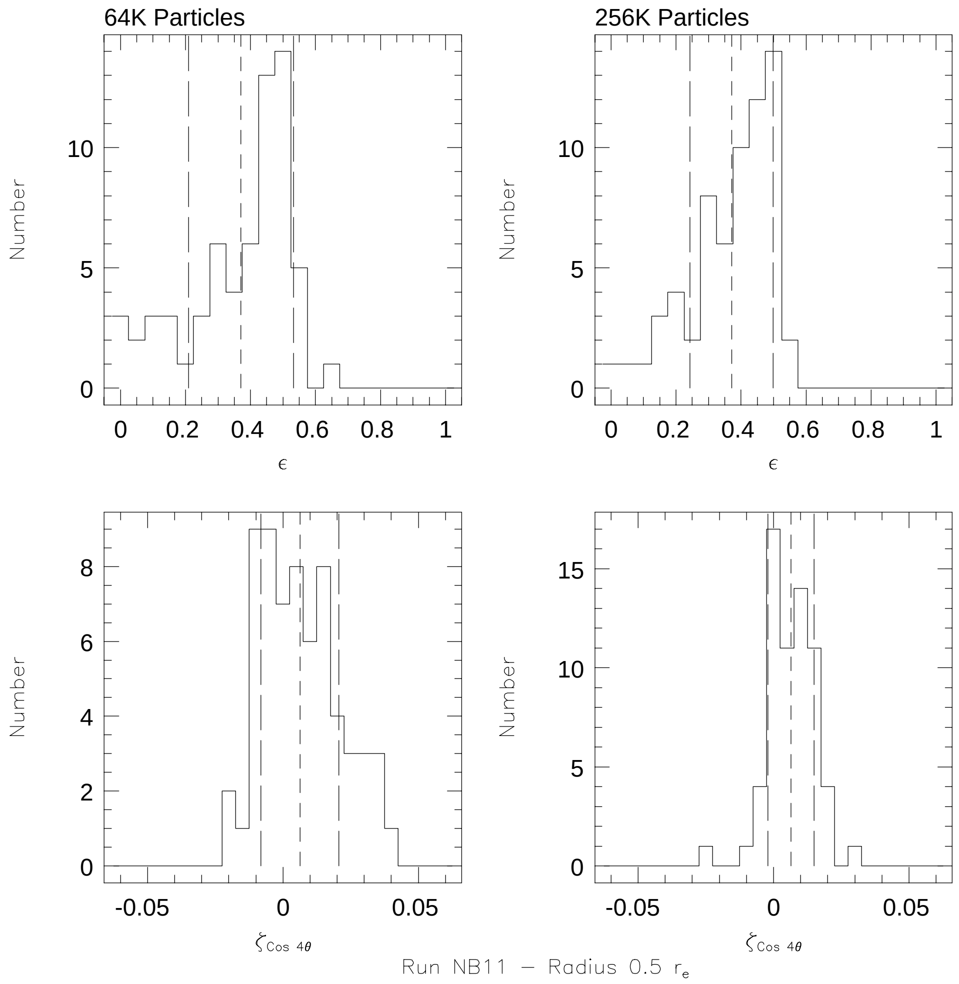

Figure 1: The four panels depict the distribution of ellipticity and $\zeta_{\cos 4\theta}$ (boxiness or diskiness) for the initial conditions `NB11` over the various orientations at one half of the half–light radius and for both the small and large simulation. To calculate these distributions, we view the remnant at the last timestep from a uniform sample of sixty-four orientations. These orientations were selected from only one quadrant of the sphere to take advantage of the symmetries of the remnant. For each of these viewpoints, an image of the remnant was created by projecting each of the luminous particles onto a 400-by-400 grid (or a 200-by-200 grid for the small simulation) which represented a region 20-by-20 length units. The number of particles in each grid square were counted and then these values were smoothed to create the image. Finally, the ellipticity and boxiness (or diskiness) were measured at the projected half–mass radius by fitting an isodensity contour to the smoothed image. Also depicted on each graph are the mean (the short-dash line) and the spread in these values (the long-dash lines) which is defined as the mean plus or minus the standard deviation of the distribution.

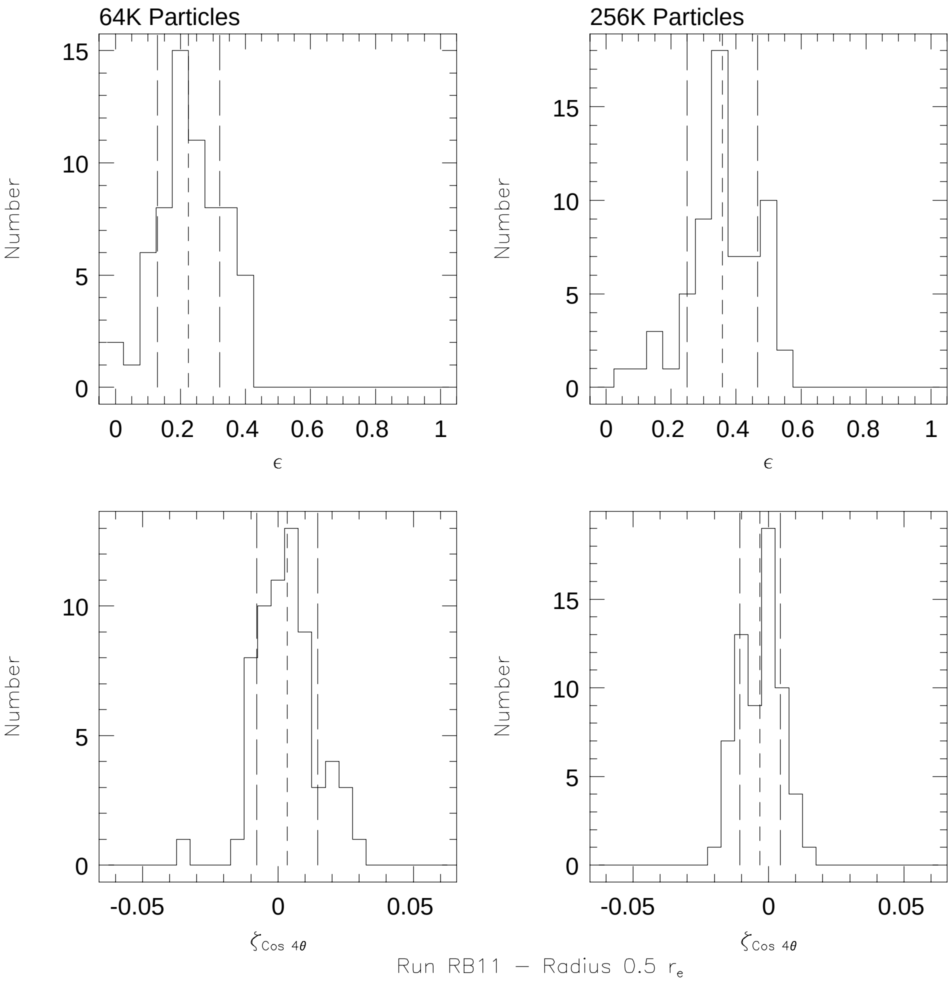

Figure 2: Figure 2 is the same as Figure 1 but for the initial conditions `RB11`.

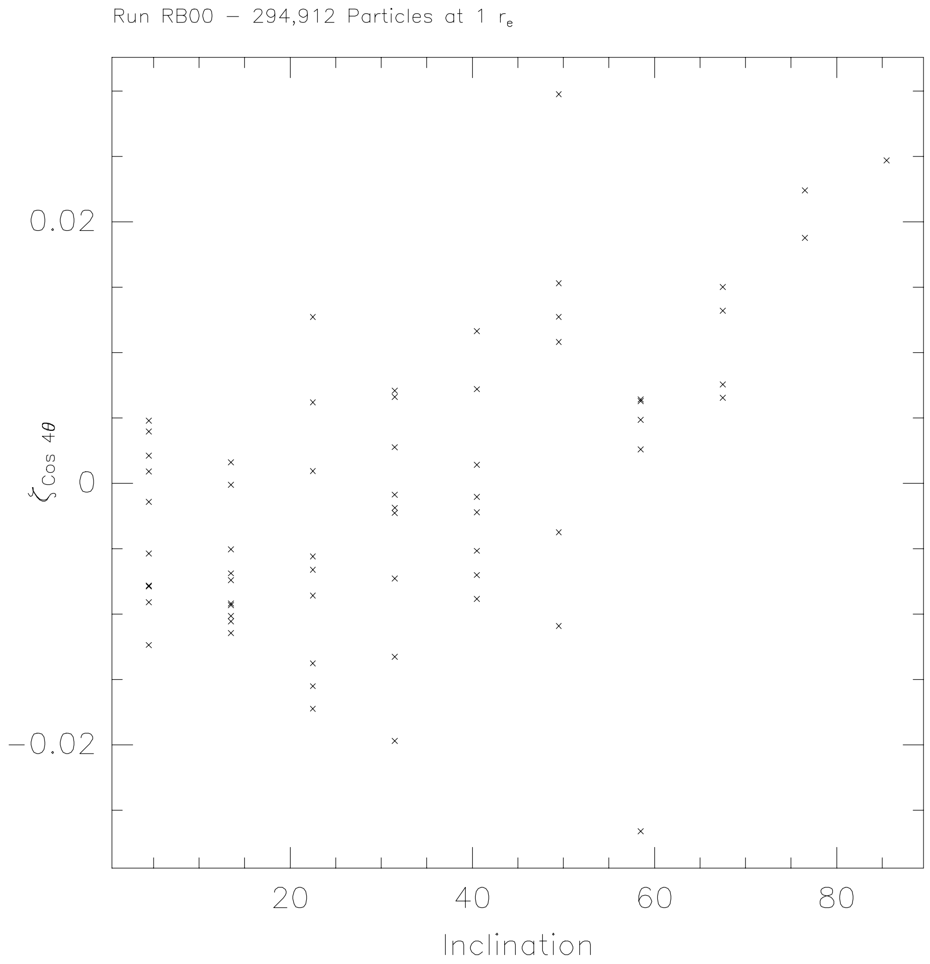

Figure 3: Figure 3 depicts $\zeta_{\cos 4\theta}$ at the half-light radius as a function of the inclination of the line of sight from the initial orbital plane for the simulation RB00 with 294,912 particles. For each inclination, the boxiness or diskiness is calculated for a variety of azimuthal angles; this results in the spread in boxiness at each inclination. These values are calculated as described in the text and in the caption to Figure 1.

especially disky, there is a slight surplus of boxy objects in the set of larger simulations. Furthermore, Figure 6 depicts the relationship between ellipticity and $\zeta_{\cos 4\theta}$. Generally, there is little correlation with the exception that all the highly flattened remnants are also boxy.

5 Discussion

5.1 Particle Number: Too Much Is Never Enough

The reason that the errors decrease both with increased particle number and with the presence of the bulge in the progenitors is simply that the ensemble of pixels used to fit the isophotes is less noisy in simulations with larger N. We could reduce counting noise in our images and therefore the errors in our analysis by performing larger simulations. We could either simply increase the total number of particles (and thus the cost in computing time), or we could add massless particles which are not included in the time–consuming calculations of the potential but would allow us to more finely sample the phase–space distribution of the remnant. Since our images are simply special projections of the phase–space they too could be more finely or alternatively less noisily sampled. The advantage of this method over simply increasing the total number of particles is that adding massless particles does not increase the computing time as drastically as increasing the size of the simulation.

When comparing the results for the 256–thousand–particle simulations and those for the smaller experiments, a second reason to use more particles in merger simulations becomes apparent. The remnants of the smaller simulations tend to be rounder and their isophotes follow ellipses less closely. We expect that more particles can more accurately follow the evolution of the merger; consequently, the isophotes in the larger experiments better describe the isophotes of merger remnants, and a further addition of particles could result in more flattened and more exactly elliptical isophotes. Unfortunately, to make the calculation of the progression of the merger more accurate, we cannot resort to the "trick" described in the previous paragraph. We must actually increase the number of massive particles in the experiment; more specifically, we should first increase the number of particles in regions of the progenitors that are most prone to errors.

5.2 Reconciliation with Observations

The isophote analysis of the twelve models leads us to make a few conclusions concerning the merger hypothesis. First, within the errors of the fitting algorithm the mergers yielded remnants with nearly equal numbers of boxy and disky isophotes when examining a variety of orientations. Although the strength of the deviations are weaker in the simulations than in the observations, these

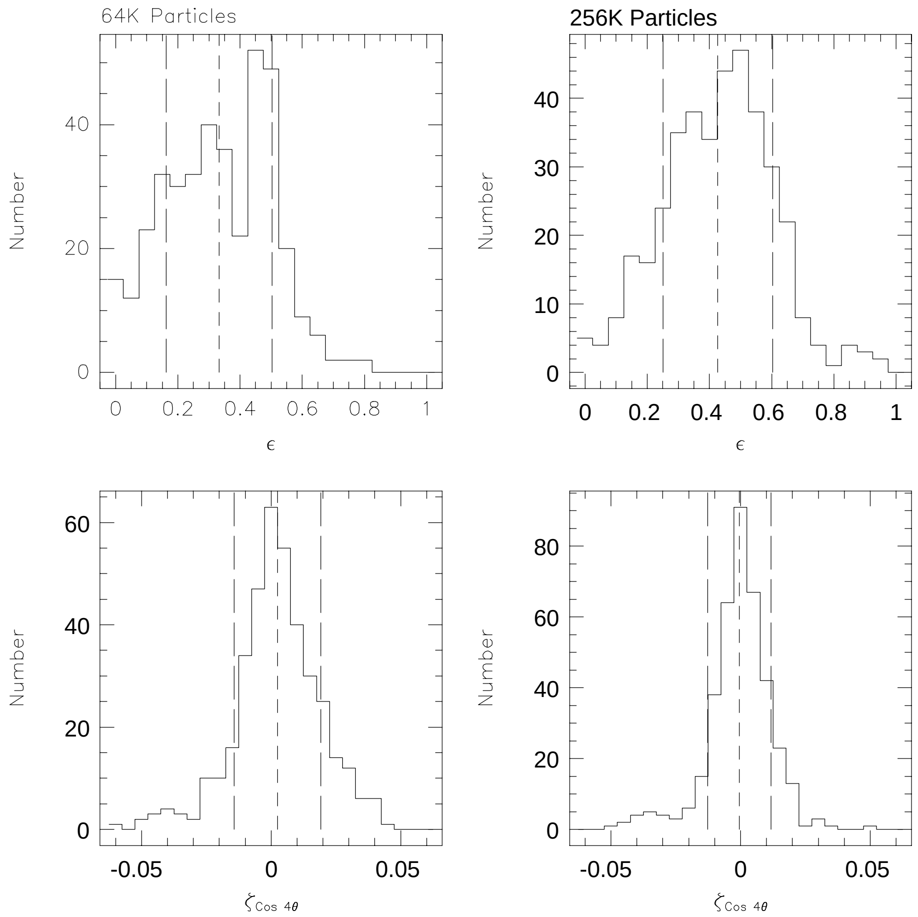

Figure 4: Figure 4 depicts the distribution of ellipticity and $\zeta_{\cos 4\theta}$ at one half the half-light radius for all the simulations and orientations discussed. Otherwise, it is similar to Figure 1.

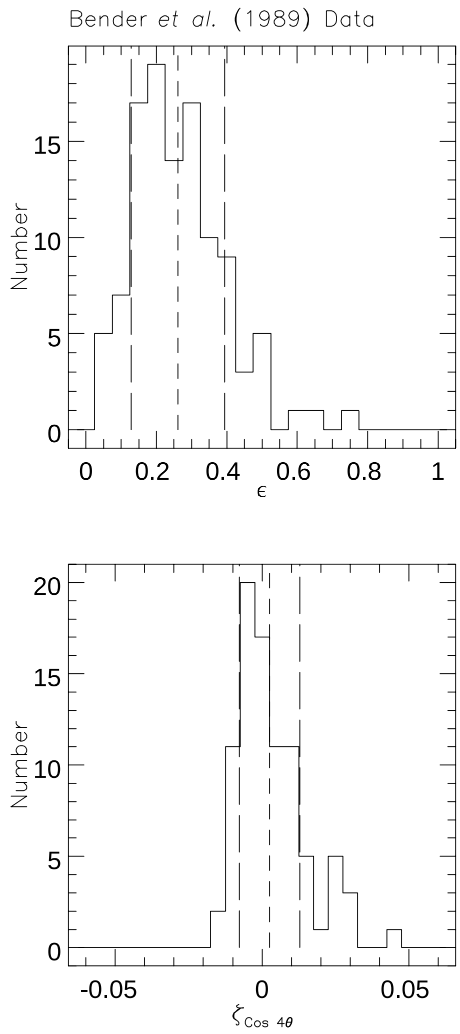

Figure 5: Figure 5 shows the distribution of ellipticity and $a(4)$ (analogous to our $\zeta_{\cos 4\theta}$ parameter) for the sample of elliptical galaxies studied by Bender *et al.* (1989). 22 of 109 galaxies have been excluded from the lower pane, because they have "irregular" isophotes (that is, isophotes which go from being boxy to disky with radius).

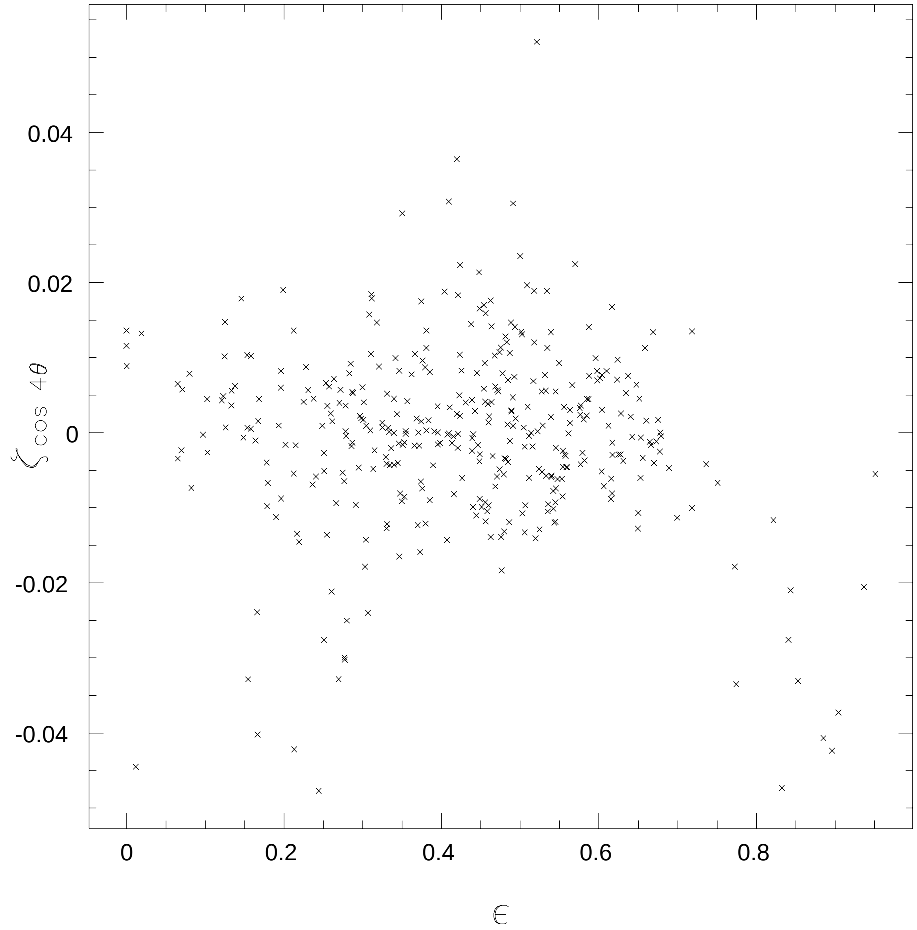

Figure 6: Figure 6 examines the relationship between ellipticity and $\zeta_{\cos 4\theta}$. In general, it appears that there is little correlation excepting the fact that most of the highly flattened remnant are also boxy.

ratios agree with the observed distribution of northern elliptical galaxies with approximately 1/3 showing boxy isophotes, 1/3 disky and 1/3 which change with radius from disky to boxy or vice versa (Bender *et al.* 1989) and with Michard & Simien (1988). Figure 5 depicts the distribution of ellipticities and residuals for the Bender *et al.* (1989) sample. By comparing this to figure 4, one can see that the remnants tend to be a bit more flattened than ellipticals observed. However, the distribution of residuals appears to be a better match.

Within the limits of the simulations, the formation of ellipticals through dissipationless mergers does not discriminate on the basis of boxiness or diskiness and cannot provide a "different track of galaxy evolution" for disky versus boxy ellipticals, as it produces both. Finally, we expect that boxiness or diskiness is a function of the orientation of the galaxies. A galaxy that appears disky from one orientation may appear boxy from another, in agreement with Franx's (1988) suggestion.

Although some of the initial conditions result in remnants with an abundance of very boxy or disky isophotes with deviations of greater than one percent, those that we believe are more likely to occur tend to produce remnants with more closely elliptical isophotes. Furthermore, the simulated mergers do not produce an overabundance of very flat remnants. Both of these conclusions agree with the observation that only a fraction of ellipticals show very boxy or disky isophotes with greater than one percent deviations (Franx 1988) and the lack of ellipticals with ellipticities greater than 0.7 (Ryden 1992).

If we suppose that ellipticals did form through mergers, we can make some predictions about the structure and origin of ellipticals. First, we would expect ellipticals to form in mergers with skew and messy initial conditions which according to the simulations result in rounder remnants with less boxiness or diskiness. Second, we would expect that the diskiness or boxiness of an elliptical galaxy to depend on orientation and distance from the center of the galaxy. However, our simulations do not rule out the possibility of a unique species of disky or boxy objects which is indicated by the observed correlations between X-ray, radio and kinematic properties and disky or boxiness (Bender *et al.* 1989). Rather they point out that a fraction of disky and boxy objects may belong to one species viewed from different orientations. Third, we would expect that elliptical galaxies like the remnants are truly triaxial, rather than perfectly oblate or prolate; thus few elliptical galaxies would appear perfectly round, in accordance with recent statistical analyses of the shapes of ellipticals (Franx *et al.* 1991, Fasano 1992).

6 Conclusion

Observations of intrinsic shapes of ellipticals are potentially a guide to determining their origin. In this paper, we explored the isophotal shapes of remnants of simulations of galaxy mergers. We find that the range of the isophotal shapes of the simulated merger remnants is roughly consistent with the observed range of isophotal shapes.

The simulations in this paper confirm Franx (1988) and Governato *et al.* (1993) conclusions that boxiness/diskiness is sensitive to galaxy orientation. The same merger remnant may appear boxy in one orientation and disky in another orientation.

The distribution of intrinsic shapes of ellipticals are another potential test of the theories of galaxy formation. Franx *et al.* (1991) has argued that the observed distribution of shapes is rounder than predicted in numerical simulations of galaxy formation with "CDM initial conditions". Hernquist (1993c) has argued that the discrepancy between the distribution of shapes predicted in mergers and the observed distribution might be even more severe with nearly planar mergers producing highly flattened ellipticals. However, the simulations suggest that mergers produce remnants whose isophotes resemble those of elliptical galaxies both in ellipticity and their deviations from ellipses, especially for the encounters that we believe are most likely to occur. Without a detailed merger scenario that predicts a distribution of merger orientations, we cannot quantitatively compare the merger simulations to the observed distribution. Thus, based on these simulations, we conclude that the distribution of isophotal shapes will probably not constrain galaxy formation in scenarios where *dissipationless* merging is predominant. More promising may be kinematic signatures, such as misalignments, rotation curves and line-of-sight velocity distributions (Heyl, Hernquist & Spergel 1993; van der Marel *et al.* 1993; van der Marel & Franx 1993; Barnes 1992), which may represent a "smoking gun" for revealing the origin of early–type galaxies.

Additionally, we transplanted the bootstrap method from the analysis of redshift surveys to determine the errors in our theoretical calculations. Bootstrapping is especially useful in the study of numerical simulations and does not involve any approximations beyond those of the simulations themselves. We believe that the bootstrap provides a valuable tool in the analysis of numerical experiments and believe that it may be applicable in a wide range of problems in numerical astrophysics.

7 Acknowledgements

This work was supported in part by the Pittsburgh Supercomputing Center, the Alfred P. Sloan Foundation, NASA Theory Grants NAGW–2422 and NAGW–2448, and the NSF under Grants ASC 93-18185, AST 90-18526, AST 91-17388, AST 88-58145 (PYI), and the Presidential Faculty Fellows Program. This work was completed as part of J.S.H.'s senior thesis and was supported by the Roundtable Senior Thesis Fund. J.S.H. also received support from the Marshall Aid Commemoration Commission. J.S.H. and D.N.S. would also like to thank the members of the department of Astronomy and Astrophysics of the

University of California – Santa Cruz for their hospitality during preparation of this work. We would like to thank Robert Lupton for a helpful discussion on bootstrap methods and Fabio Governato and Ralf Bender, our referee, for many insightful comments on an earlier version of this manuscript.

8 References

Bahcall, J.N. & Soneira, R.M. 1980, ApJS 44, 73.
Barnes, J. & Hernquist, L. 1992, ARA&A 30, 705.
Barnes, J. & Hut, P. 1986, Nature 324, 446.
Barnes, J.E. 1988, ApJ, 331, 699.
Barnes, J.E. 1992, ApJ, 393, 484.
Bender, R. 1988, A&A 202, L5.
Bender, R. 1990, A&A 229, 441.
Bender, R., Burstein, D., & Faber, S.M. 1992, ApJ 399, 462.
Bender, R., Burstein, D., & Faber, S.M. 1993, ApJ 411, 153.
Bender, R., Döbereiner, S., & Möllenhoff, C. 1987, A&A 177, L53.
Bender, R., Surma, P., Döbereiner, S., Möllenhoff, C. & Madejsky R. 1989, A&A, 217, 35.
Bertola, F. & Capaccioli, M. 1975, ApJ, 200, 439.
Bhavsar, S.P. 1990, in Errors, Bias and Uncertainties in Astronomy, eds. C. Jaschek and F. Murtagh, 107 (Cambridge Univ. Press, Cambridge).
de Vaucouleurs, G. 1948, Ann. d'Astrophys., 11, 247.
de Zeeuw, T. & Franx, M. 1991, ARA&A, 29, 239.
Djorgovski, S. & Davis, Marc 1987, ApJ, 313, 59.
Dressler, A., Lynden-Bell, D., Burstein, D., Davies, R.L., Faber, S.M., Terlevich, R. & Wegner, G. 1987, ApJ, 313, 42.
Efron, B. 1979, Ann. Stat., 7, 1.
Fasano, G. 1992, MNRAS, 249, 208.
Franx, M. 1988, Structure and Kinematics of Elliptical Galaxies, PhD Thesis.
Franx, M. & Illingworth, G. 1988, ApJ, 327, L55.
Franx, M. & Illingworth, G. 1990, ApJ, 359, L41.
Franx, M., Illingworth, G., & Heckman, T. 1989, ApJ, 344, 613.
Franx, M., Illingworth, G. & de Zeeuw, T. 1991, ApJ, 383, 112.
Governato, F., Reduzzi, L. & Rampazzo, R. 1993, MNRAS, 261, 379.
Hernquist, L. 1987, ApJS 64, 715.
Hernquist, L. 1990a, J. Comput. Phys. 87, 137.
Hernquist, L. 1990b, ApJ 356, 359.
Hernquist, L. 1992, ApJ 400, 460.
Hernquist, L. 1993a, ApJ 409, 548.
Hernquist, L. 1993b, ApJS 86, 389.
Hernquist, L. 1993c, in The Evolution of Galaxies and Their Environment, ed. H. Thronson, in press.

Hernquist, L., Heyl, J.S. & Spergel, D.N. 1993, ApJ, 416, L9.
Hernquist, L. & Katz, H., ApJS 70, 419.
Hernquist, L. & Spergel, D.N. 1992, ApJ 397, L117.
Hernquist, L., Spergel, D.N. & Heyl, J.S. 1993, ApJ, 416, 415.
Heyl, J.S., Hernquist, L., & Spergel, D.N. 1993, in preparation.
Illingworth, G. 1977, ApJ, 218, L43.
Jedrzejewski, R.I. 1987, MNRAS, 226, 747.
Jedrzejewski, R.I. & Schechter, P.L. 1988, AJ, 98, 147.
Lupton, R.H. 1993, Statistics in Theory and Practice, Princeton University Press, in press.
Malin, D.F. & Carter, D. 1980, Nature, 285, 643.
Malin, D.F. & Carter, D. 1983, ApJ, 274, 534.
Michard, R. & Simien, F. 1988, A&AS, 74, 25.
Nieto, J.-L., Bender, R., & Surma P. 1991, A&A 244, L37.
Nobelis, Ph.P. 1990, in Errors, Bias and Uncertainties in Astronomy, eds. C. Jaschek and F. Murtagh, 89 (Cambridge Univ. Press, Cambridge).
Peletier, R.F. *et al.* 1990, AJ, 100, 1091.
Press, W.H., Rybicki, G.B. & Schneider, D.P. 1993, CfA preprint 3601, to appear in ApJ.
Rix, H.-W. & White, S. 1992, MNRAS, 254, 389.
Ryden, B. 1992, ApJ, 396, 445.
Schweizer, F. 1980, ApJ, 237, 303.
Simien, F. & Michard, R. 1990, A&A, 227, 11.
Spergel, D.N. & Hernquist, L. 1992, ApJ 397, L75.
Stiavelli, M., Londorillo, P. & Messina A. 1991, MNRAS 251, 57p.
Toomre, A. 1977, in The Evolution of Galaxies and Stellar Populations, eds. B. Tinsley and R. Larson, 401 (Yale Univ. Press, New Haven).
Toomre, A. & Toomre, J. 1972, ApJ 178, 623.
van der Marel, R.P. & Franx, M. 1993, ApJ 407, 525.
van der Marel, R.P., Rix, H.-W., Carter, D., Franx, M., White, S.D.M., & de Zeeuw, T. 1993, MNRAS, submitted.